Bulletin of the Seismological Society of America, 91, 4, pp. 753–759, August 2001

Kursk Explosion

by Brian Savage and Don V. Helmberger

Abstract On 12 August 2000 two explosions damaged the Russian submarine, the Kursk. The largest event was well recorded at seismic networks in northern Europe, which we then modeled. We developed a hybrid method based on generalized ray theory that treats an explosive source embedded in a fluid and recorded along continental paths. Matching record sections of observations with synthetics, we obtain an estimate of explosive size of slightly over 4 t. Several earth models determined previously, K8 and a Baltic model, were used to assess accuracy. These results are in general agreement with other investigators using more empirical methods. Knowing the conventional missile yield and the explosion size allows for an estimate of approximately five missiles exploded in the second larger explosion onboard the Kursk.

Introduction

On 12 August 2000, two events were located in a seismically inactive region, less than 10° from Novaya Zemlya, where a large number of nuclear tests were conducted over the decades. These events were located close together in the Barents Sea region at shallow depths, the latter measuring m_b 3.5. Figure 1 shows the location of the larger event and stations used in the analysis. A few days after the events occurred, news agencies reported that a Russian submarine, the Kursk, had been damaged during exercises in the Barents Sea. The seismic events were located in the same region and at the same time as when the Kursk reportedly sunk.

The Kursk is a Russian nuclear submarine, Oscar II class, with the ability to carry 24 antiship cruise missiles. While the missiles can be nuclear in nature, 500 kt, it is more likely that those carried on the Kursk were a conventional explosive size of 750 kg (∼.75 t) (Bellona Foundation, 2000), as the nuclear warheads have been placed into storage. A single missile of this size, exploded underwater, is easily capable of generating seismic waves that can travel local distances. Given low attenuation, the same missiles can be detected regionally, while multiple missile explosions can generate energy that has the ability to travel much further. Being that the time and spatial extent of the events match those of the damaged Kursk, and that there was an explosive capability most likely present at the time of the events, leads us to the conclusion that the two events recorded seismically and the damage to the Kursk are related.

Our main purpose in this article is to get a better understanding of what happened onboard the Kursk in terms of the size of the explosions. A few techniques have been utilized to determine the size of underwater explosions, which include using various magnitude scales or characteristics in the amplitude spectra (Gitterman and Shapira, 1994; Baumgardt and Der, 1998; Gitterman *et al.,* 1998; Koper *et al.,* 2001). However, the approach taken in this article will be to use synthetic waveforms to understand more about the seismic signatures in the time domain. The observations (short-period, 0.2–20 Hz, vertical field) are displayed in Figure 2, plotted as a reduced section which aligns the Pn. We have included some reference lines to aid in the phase identification. Since we see frequencies of 3 Hz at distances over 900 km, it is most likely the case that attenuation does not play a very important factor. Additionally, there is little to no apparent frequency shift as we proceed out in distance, reinforcing this point. Moreover, no large amplitude variation with azimuth is seen, as is characteristic of an explosion.

In this study, we address the extended *P*-wave motions because most of our knowledge about crustal structure is for *P* waves. A discussion of the relationship between *P* and *S* waves in our data will be reserved until later, as they are intimately related to the water in which they are produced. In order to compute synthetics for an underwater explosion, we will first characterize an underwater explosive source, and then describe seismic-wave propagation within a water layer. Finally, we will compare the synthetics to the waveform data in an attempt to estimate explosion size.

Underwater Explosive Sources

Following the descriptions by Weston (1960), Arons (1954), and Cole (1948), the time dependence of pressure of an underwater explosion can be formulated. Note that a single explosion in water is comprised of a series of overpressures and underpressures caused by the pulsation of the gas volume in the water. Examples of the gas volume pulsation can be seen in the article by Helmberger (1968). These overpressures, or bubble pulses, essentially act as new sources,

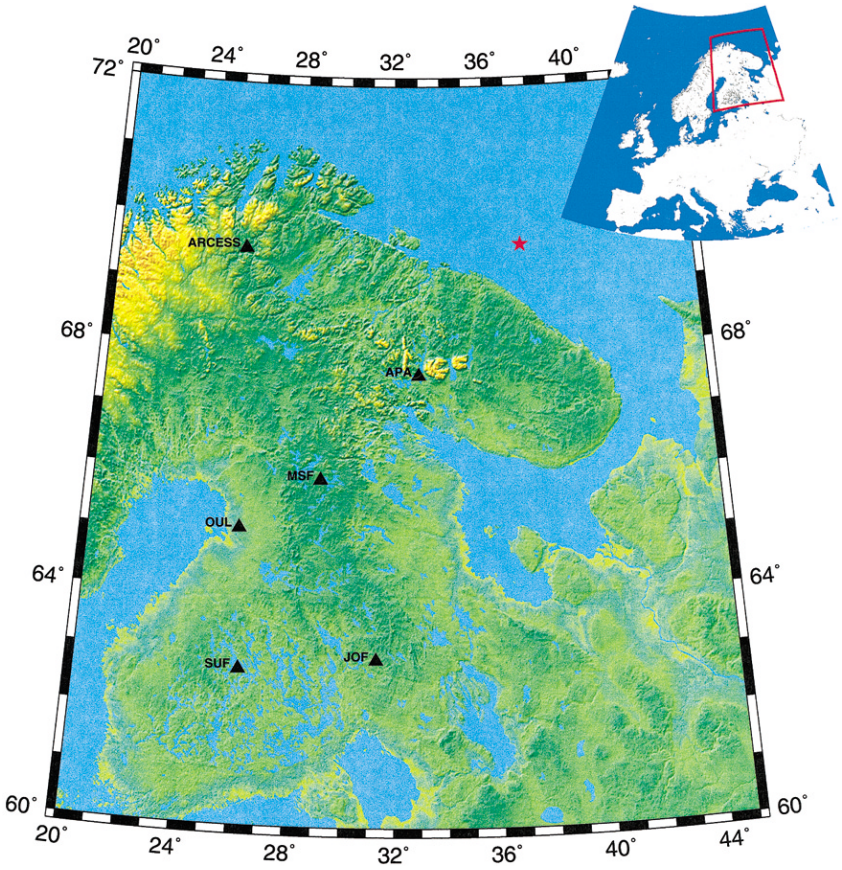

Figure 1. Map of the region surrounding the Kursk explosion (star) and stations (triangles) used in determining the explosion size.

and their relative amplitude is dependent on detonation depth and explosive yield. The relation between the peak pressure and the explosive yield for the first pulse is shown by Weston (1960) as

$$P_0 = 2.16 \times 10^4 \left[\frac{Y_0^{1/3}}{r}\right]^{1.13}$$

where P_0 is in dyne/cm^2, Y_0 is the yield is in pounds of trinitrotoluene (TNT), and r the distance from the source to the receiver, is in feet. The overpressures decay as an exponential where the relaxation time of the initial pulse is defined by

$$t_0 = 1/\alpha = 58 Y_0^{1/3} \left[\frac{Y_0^{1/3}}{r}\right]^{0.22}$$

The underpressures occur over a much greater time period and return the pressure of the region back to a hydrostatic level. As will be shown later, as the yield increases, the effect of the later pulses on the final waveforms decreases dramatically. To simplify the calculation, only the first pulse will be used in the characterization of the source. Later, we will add the bubble pulses as secondary effects. The underwater source description, classically defined in units of pressure, needs to be defined in units of displacement potential for synthetics to be computed.

Following the formulation of a simple source with no radiation pattern (Helmberger, 1983), we define the the pressure of the initial pulse by

$$P(t) = \frac{R_0}{R} P_0 e^{-\alpha(t-R/c)} H\left(t - \frac{R}{c}\right),$$

where P_0 is the maximum pressure of the initial pulse, α is the half-width of the initial pulse in inverse sec, R and R_0 are distances where R_0 is set to a reference distance of 1 km, and c is the fluid velocity. We then define the displacement potential ϕ in terms of the pressure as

$$P(t) = \frac{R_0}{R} P_0 e^{-\alpha(t-R/c)} = \rho \frac{\partial^2 \phi(t)}{\partial t^2},$$

where ρ is the density, and ϕ has units of length^2. Solving for the displacement potential is a simple double integration with the initial and final conditions of

$$\phi\left(t - \frac{R}{c} = 0\right) = 0, \text{ and}$$
$$\int P(t)dt = 0.$$

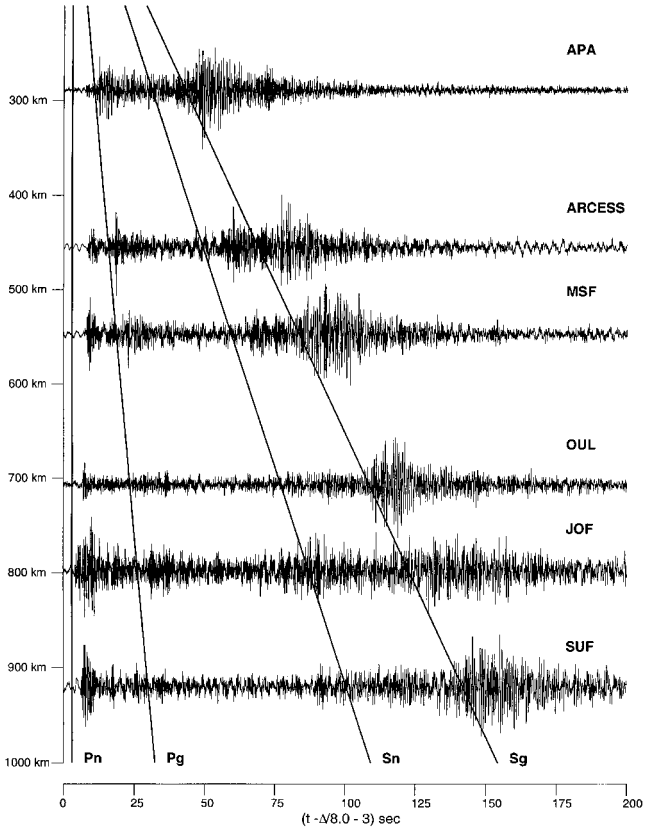

Figure 2. Short-period (0.2–20 Hz) vertical data from stations shown in Figure 1. Note the relative similar amplitudes between *P* and *S* arrivals. Lines for theoretical arrival times of *Pn*(8.0 km/sec), *Pg*(6.7(km/sec), *Sn*(4.7 km/sec) and *Sg*(4.0 km/sec) are also shown for reference.

The first condition constrains there to be no motions before the arrival of the initial pulse, while the second allows for the pressure at long times to return to the hydrostatic level.

Therefore the final relation for the displacement potential is

$$\phi(t) = \frac{P_0}{\rho\alpha^2}\frac{R_0}{R}(e^{-at} - 1),$$

with the reduced displacement potential, ψ, defined as

$$\psi(t) = -R\phi(t) = -\frac{P_0}{\rho\alpha^2}R_0(\mathrm{e}^{-at} - 1).$$

Waveform Modeling

After some manipulation of the underwater explosive displacement potential, ϕ, and the Green's functions, $S(t)$, we can create synthetic displacement waveforms for underwater explosions. To obtain displacement from the explosion displacement potential, a derivative with respect to distance, R, of ϕ must be taken, as

$$D(R, t) = \frac{d\phi(t)}{dR} = \frac{1}{R^2}\psi(t) + \frac{1}{cR}\frac{d\psi(t)}{dt}.$$

The first term in the relation for displacement describes displacement in the near-field and acts as a ramp function, whereas the second term describes the displacement in the far-field, which is similar to a delta function.

Keeping only the far-field term, following the derivation discussed by Helmberger (1981, 1983), and keeping in mind $r \neq R$, we obtain

$$D(r, z, t) = \left(\frac{d\psi(t)}{dt} \times \frac{dS(t)}{dt}\right),$$

where

$$S(t) = \sqrt{\frac{2}{r}}\frac{1}{\pi}\left[\frac{1}{\sqrt{t}} \times \sum \text{rays}\right].$$

To treat the problem here we need to begin in a thin water layer with a relatively thin crust and end at the surface of a continental crust. To proceed we use a modification of generalized ray theory, similar to that discussed by Ni *et al.* (2000), that allows different source and receiver structure. Thus, we can easily include reverberations in a water layer. Inclusion of the 100-m water layer is done solely on the source side by specifying the water as an actual, but small, layer with compressional and shear velocities of 1.5 and 0.0 km/sec and a density of 1.0 g/cm^3.

We used two velocity models, specified in Table 1, to create synthetics. The Baltic model (Bondar and Ryaboy, 1997) is a model based on travel times for the Baltic shield region, while the K8 model (Given and Helmberger, 1980) is derived from WWSSN waveform modeling of explosions. Most likely the Moho is not flat for paths we are considering, and not knowing the crustal thicknesses under the source and receiver, we used simple, flat-layered crust of 25 km, rather than a more complex one. Using this simple model and a mapping technique from Zhao and Helmberger (1993), the amplitudes and travel times are preserved for differing crustal thicknesses beneath the source and receiver. The short-period *Pn*/*Pg* synthetic seismograms, for a suite of source sizes, generated at station ARCESS are displayed, along with observations, in Figure 3. Differences between the full description of the source with bubble pulses included, and the single pulse approximation, or simple decaying exponential, are also shown. The left column of Figure 3 is the complete source, while the right column only contains the approximation. It is difficult to identify characteristics of the bubble pulse in the time domain, whereas it is relatively simple in the frequency domain.

Table 1
Two Velocity Models Used to Create Synthetics

Depth (km)*	K8†	Baltic†
0	6.200	6.2000
10	6.700	6.7000
25	8.170	8.0000
40	8.170	8.0000
50	8.178	8.0000
55	8.178	8.1500
60	8.205	8.1570
70	8.222	8.2570
80	8.239	8.3286
90	8.256	8.4000
100	8.274	8.0000
110	8.291	8.0000
115	8.291	8.4200
120	8.308	8.4262
130	8.325	8.4262
135	8.325	8.4446
140	8.343	8.4446
150	8.250	8.4631
155	8.180	8.4631
160	8.050	8.4631
165	8.050	8.4815
170	8.040	8.4815
180	8.150	8.5000

*Depths are at the top of the layer.
†*P*-wave velocity in km/sec.

As seen for both the synthetics and data shown in Figure 3, an extended coda is present for the *Pn* and *Pg* arrivals. The existence of these arrivals is due entirely to extended water reverberations and not the bubble pulse. A water layer, in relation to the solid earth, is a low velocity layer that can trap seismic energy. Multiple water reverberations are distinct arrivals and can be the most prominent arrivals on regional records, as seen in the data. The frequency of the water reverberations is defined by Gitterman *et al.* (1998) as

$$f_w = \frac{c}{4h_w},$$

where c is the wave velocity in water, and h_w is the water height. Using a wave velocity of 1.5 km/sec and a h_w of 100 m, the frequency of reverberations becomes 3.75 Hz, similar to the data. This extended coda is present throughout the entire record, including *P* and *S* waves, as seen in Figure 2.

Examining the entire record further, the *P*-arrival strengths exhibit a signal comparable to those for *S*-arrivals. Since the *S* waves contain water reverberations and the source-derived bubble pulses, they can be used in the whole record spectral analysis discussed previously as a discriminant. Another discriminant utilizes the amplitude ratio of particular phases, namely *Pn, Pg, Sn*, and *Sg*, commonly known as *Lg*. Identification of the phase *Sn* is difficult in Figure 2, although a relatively strong complex *Sg* is evident. This phenomenon of weak *Sn*, when compared to *Sg* or *Pn*, is common in oceanic exploration with soft bottom sediments (Helmberger and Morris, 1970). A ratio of the larger amplitude phases, *Pn* and *Sg*, for this event is slightly smaller than those reported in Baumgardt and Young (1990) for underwater explosions, although this difference is again likely due to the amount of mud and silt on the seafloor beneath the explosion. Another comparison of the *Pn*/*Sg* ratio for

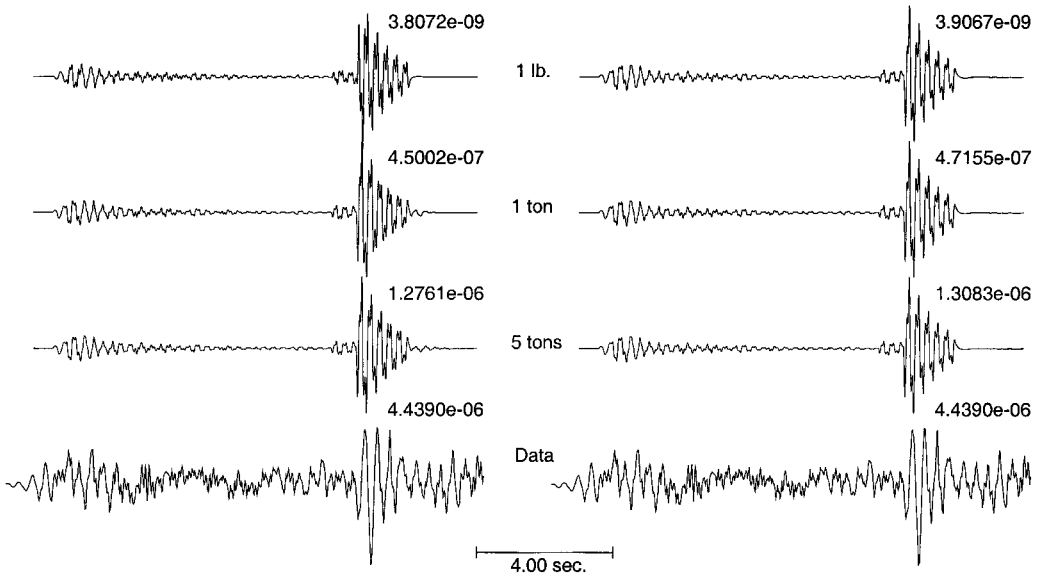

Figure 3. *Pn*/*Pg* synthetics created for the full description of the source (first column), and the first pulse approximation (second column). The first three rows are synthetics for explosive sizes of 1 lb., 1 ton, and 5 ton, with amplitudes in cm. The last row is the data recorded at station ARCESS. Waveform shape differences in the final synthetics are only seen for small yields, while larger yields differ only in amplitude.

this event, ~1.0, with earthquakes in this region, ~0.5, is similar to those reported by Baumgardt and Young (1990) and Dysart and Pulli (1990). Again, while the water layer affects the character and amplitude of the *P* and *S* arrivals in the time domain, the bubble pulse signal will dominate in the frequency domain, but identification in waveforms is difficult.

Turning back to Figure 3, the largest differences between waveforms with and without the bubble pulse is easily seen at small yields. While large yields only differ in amplitude, the smaller yields have a modified waveform shape. In this example, the *Pg* arrivals are of opposite polarity compared to larger shots. This is entirely due to the interference produced between the initial explosion and the bubble pulse. Shown in Figure 4 are pressure time series computed for a ranges of sizes. The pressure series have been convolved with a double-sided instrument response that accentuates their impact. As shown by Weston (1960), the timing of the bubble pulse shifts toward the initial pulse as the explosion size decreases. Therefore, for smaller-sized sources, detonated at a constant depth, the bubble pulse interferes with the initial pulse to create complicated waveforms.

Waveform data used in this study have amplitudes comparable to to those from an explosion greater than 1 t. Knowing this, we can only use the amplitude of the waveform to determine the size, because at large yields the waveform shape does not change. A comparison of synthetics at 1 ton for the two models against all the observations are given in Figure 5. For comparison, the synthetics are convolved with the same instrument that recorded the data. Each model fits the arrival time and energy envelopes at distances greater than 650 km, but the K8 model explains the arrival times and relative *Pn*/*Pg* amplitudes at APA and ARCESS better than the Baltic model. Both models show characteristics not seen in the data for larger distances. Around 700 km, the Baltic model's upper mantle produces a critically reflected arrival resulting in larger than expected amplitudes, whereas the K8 model has a large secondary arrival, coming from the top of the low velocity zone, 5 sec following the initial arrival.

Although we would expect to see an impulsive compressional first motion, positive on the vertical component, most observations appear to be either weak or negative. At smaller distances, the synthetics from both models are positive, but as the distance increases, the first arrival becomes weak or negative. More distant recordings sample a greater extent of the lid structure. To accurately model this set of data, with a large percentage of energy centered around 3 Hz, we need to know the very fine structure of the lid within a few kilometers. These models in Table 1, derived from travel-time data, do not have the resolution required to model at the required frequencies.

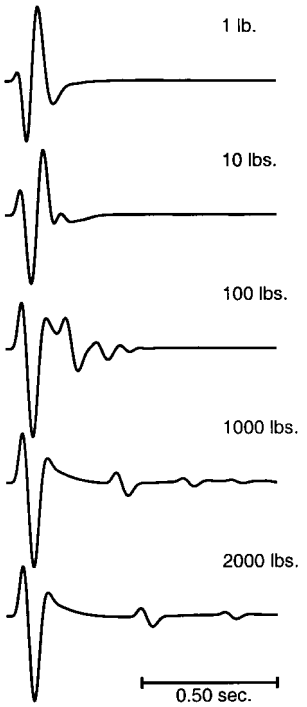

Figure 4. Pressure time series convolved with an instrument response for a series of explosive sizes. Note how the later pulses interfere with the initial pulse as the shot size decreases.

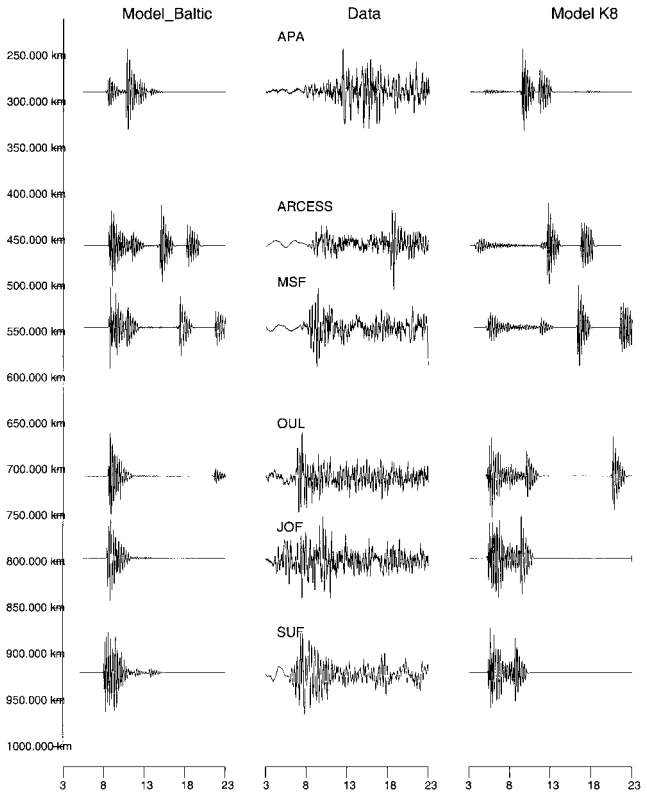

Figure 5. Record section of data, in the center column, and synthetics for the two velocity models used in this study. The peak amplitude considerations are given in Figure 6.

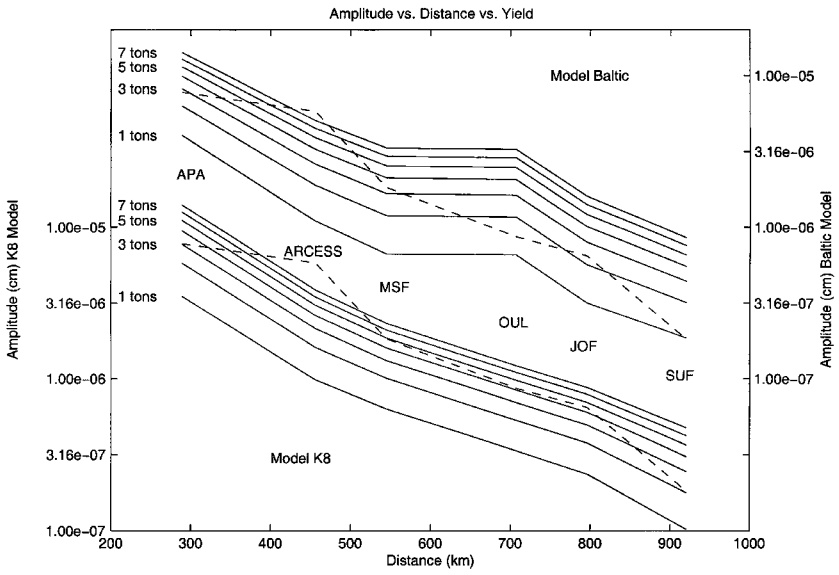

Figure 6. Maximum *P* amplitude (cm) plotted versus distance and yield. The top set of curves are for the Baltic model and has its axis on the right, while the bottom set corresponds to the K8 model and has its axis on the left. The data for each is the dotted line, and the solid lines are maximum amplitudes from 1 to 7 ton shots, increasing by 1 ton for each line.

Synthetics for the K8 and Baltic models are computed for a range of different yields from 1 lb. to 50 t. From these synthetics, the maximum *P*-wave amplitudes are plotted against those from the data in Figure 6. This data shows the larger explosion had a yield of slightly over 4 t, in mean and median using the K8 model. The Baltic model, on the other hand, predicts a smaller yield between 2 and 3 t. Unfortunately, the smaller explosion's signal-to-noise ratio is too small to determine a yield using this method. Other classical methods of explosion size determination, employed by Koper *et al.* (2001) for the same explosion, show a range similar yields of approximately 4 t.

If we then assume the Kursk was carrying missiles with a conventional explosive yield of 750 kg and the explosion was slightly more than 3628 kg, then about five missiles exploded in the large explosion. Knowing the size of the nuclear warheads, we can conclude that no nuclear warheads were detonated in the explosion. Knowing the size of the first and smaller explosion would give us a better insight into what the original cause of incident was.

Conclusion

We have estimated the size of the second larger explosion onboard the Russian submarine, the Kursk. Our new method obtains a yield of slightly larger than 4 t (3628 kg), equaling about five missiles at 750 kg each. By employing this new method of matching amplitudes of synthetics to those of seismic waveform data, we can recover the size that agrees with other methods. By using this method and time domain records, more information about underwater explosions can be extracted. First, the recorded waveforms show that the largest amplitudes arrivals are due to successive water reverberations and not the bubble pulse. Secondly, the secondary sources become unimportant in the time domain, when the yield exceeds a threshold. Next, the relative amplitude of *P* to *S* can be used as a discriminant for explosions in water. Along with the *P* to *S* ratio, identification of bubble pulses in the frequency domain and water reverberations in the time domain can act in concert to discriminate an underwater explosion from an earthquake. Finally, we have developed a method of creating synthetics for underwater explosions describing the source and how the seismic waves propagate within a water layer.

Acknowledgments

We would like to thank Brad Woods, Hong-Kie Thio, Chandan Saikia, Jascha Polet, and two anonymous reviewers for their reviews, Ralph Alewine for his suggestion to attempt this work numerically, Terry Wallace and Keith Koper for their discussions and data from the University of Arizona, Tucson, and finally Hans Israelsson and Ulf Baadshaug for waveform data. This research was supported by the Defense Threat Reduction Agency under Contract DSWA01-98-1-0010. This is Contribution No. 8745, Division of Geological and Planetary Sciences, California Institute of Technology, Pasadena, California.

References

Arons, A. B., J. P. Slikko, and A. Carter (1948). Secondary pressure pulses due to gas globe oscillation in underwater explosions. I. Experimental data, *J. Acoust. Soc. Am.* **20,** no. 1, 271–276.

Arons, A. B. (1948). Secondary pressure pulses due to gas globe oscillation in underwater explosions. II. Selection of adiabatic parameters in the theory of oscillations, *J. Acoust. Soc. Am.* **20,** no. 1, 277–282.

Arons, A. B. (1954). Underwater explosion shock wave parameters at large distances from the charge, *J. Acoust. Soc. Am.* **25,** no. 3, 343–346.

Bellona Foundation (2000). *http://www.bellona.no,* Bellona Foundation, Oslo, Norway.

Baumgardt, D. R., and G. B. Younf (1990). Regional seismic waveform discriminants and case-based event identification using regional arrays, *Bull. Seism. Soc. Am.* **80,** 1874–1892.

Baumgardt, D. R., and Z. Der (1998). Identification of presumed shallow underwater chemical explosions using land-based arrays, *Bull. Seism. Soc. Am.* **88,** 581–595.

Bondar, I., and V. Ryaboy (1997). Regional travel-times tables for the Baltic shield region, CMR Technical Report, Vol. 24.

Cole, R. H. (1948). *Underwater Explosions,* Princeton University Press, Princeton, New Jersey.

Dysart, P. S., and J. J. Pulli (1990). Regional seismic event classification at the NORESS array: seismological measurements and the use of trained neural networks, *Bull. Seism. Soc. Am.* **80,** 1874–1892.

Gitterman, Y., A. Shapira (1994). Spectral characteristics of seismic events off the coast of Levant, *Geophys. Jour. Int.* **116,** 485–497.

Gitterman, Y., Z. Ben-Avraham, and A. Ginzburg (1998). Spectral analysis of underwater explosions in the Dead Sea, *Geophys. J. Int.* **134,** 460–472.

Given, J. W., and D. V. Helmberger (1980). Upper mantle structure of northwestern eurasia, *J. Geophys. Res.* **85,** no. B12, 7193–7194.

Helmberger, D. V. (1968). The Crust Mantle Transition in the Bering Sea, *Bull. Seism. Soc. Am.* **58,** no. 1, 179–214.

Helmberger, D. V., and G. B. Morris (1970). A travel time and amplitude interpretation of a marine refraction profile: transformed shear waves, *Bull. Seism. Soc. Am.* **60,** no. 2, 593–600.

Helmberger, D. V., and D. G. Harkrider (1972). Seismic source descriptions of underground explosions and a depth discriminate, *J. Geophys. Res. Astron.* **31,** 45–66.

Helmberger, D. V. (1973). Numerical seismograms of long-period body waves from seventeen to forty degrees, *Bull. Seism. Soc. Am.* **63,** no. 2, 633–646.

Helmberger, D. V., and D. M. Hadley (1993). Seismic source functions and attenuation from local and teleseismic observations of the NTS events Jourm and Handley, *Bull. Seism. Soc. Am.* **71,** no. 1, 51–67.

Helmberger, D. V. (1983). Theory and application of synthetic seismograms earthquakes: observation and interpretation, *Soc. Italiana di Fisica* **85,** 174–222.

Helmberger, D. V., G. Engen, and S. Grand (1985). Upper-mantle cross-section from California to Greenland, *J. Geophys.* **58,** 92–100.

Koper, K. D., T. C. Wallace, S. R. Taylor, H. E. Hartse (2001). Forensic seismology and the sinking of the Kursk, *EOS* **92,** no. 4.

Khalturin, V. I., T. G. Rautian, and P. G. Richards (1998). The seismic strength of chemical explosions, *Bull. Seism. Soc. Am.* **88,** no. 6, 1511–1524.

Lay, T., D. V. Helmberger, and D. G. Harkrider (1984). Source models and yield-scaling relations for underground nuclear explosions at amchitka island, *Bull. Seism. Soc. Am.* **74,** no. 3, 843–862.

Ni, S., X. Ding, and D. V. Helmberger (2000). Constructing synthetics from deep earth tomographic models, *Geophys. J. Int.* **140,** 71–82.

Weston, D. E. (1960). Underwater explosions as acoustic sources, *Proc. Phys. Soc.* **76,** no. 2, 233–249.

Willis, D. E. (1963). Seismic measurements of large underwater shots, *Bull. Seism. Soc. Am.* **53,** no. 4, 789–809.

Zhao, L., and D. V. Helmberger (1993). Upper mantle compressional velocity structure beneath the northwest Atlantic Ocean, *J. Geophy. Res.* **98,** no. B8, 14,185–14,196.

Seimsological Laboratory
Division of Geological and Planetary Sciences
Mail Code 252-21
California Institute of Technology
Pasadena, California, 91125

Manuscript received 12 December 2000.